

# Synthetic gauge flux and Weyl points in acoustic systems

Meng Xiao<sup>†</sup>, Wen-Jie Chen<sup>†</sup>, Wen-Yu He and C. T. Chan<sup>★</sup>

**Following the discovery of the quantum Hall effect<sup>1,2</sup> and topological insulators<sup>3,4</sup>, the topological properties of classical waves began to draw attention<sup>5–21</sup>. Topologically non-trivial bands characterized by non-zero Chern numbers are realized through either the breaking of time-reversal symmetry using an external magnetic field<sup>5–7,15,16</sup> or dynamic modulation<sup>8,17</sup>. Owing to the absence of a Faraday-like effect, the breaking of time-reversal symmetry in an acoustic system is commonly realized with moving background fluids<sup>20,22</sup>, which drastically increases the engineering complexity. Here we show that we can realize effective inversion symmetry breaking and create an effective gauge flux in a reduced two-dimensional system by engineering interlayer couplings, achieving an acoustic analogue of the topological Haldane model<sup>2,23</sup>. We show that the synthetic gauge flux is closely related to Weyl points<sup>24–26</sup> in the three-dimensional band structure and the system supports chiral edge states for fixed values of  $k_z$ .**

Sound is probably the ‘simplest’ of all classical waves. It has no intrinsic spin and does not respond to magnetic fields; hence, the fundamental interactions underlying the quantum spin Hall effect (QSHE) and quantum Hall effect (QHE) do not apply to acoustic waves. However, by engineering the coupling in the  $z$  direction, we can create synthetic staggered flux and hence  $k_z$ -preserved unidirectional edge modes in the  $x$ - $y$  plane in acoustic meta-crystals which have simple ‘static’ structures with no moving fluid and no dynamic modulation. The acoustic meta-crystals have Weyl points<sup>24–26</sup> in the three-dimensional (3D) band structure, and the systems are acoustic analogues of the topological Haldane model<sup>2,23</sup> for fixed values of  $k_z$ .

## Tight-binding model

To illustrate how the idea works, we start with a simple nearest-neighbour tight-binding model for an AA-stacked honeycomb lattice (Fig. 1a). Its acoustic implementation will be discussed later. The Hamiltonian  $H$  of this system consists of the intralayer part  $H_0$  and the interlayer part  $H_1$ .

$$H_0 = \sum_{i,k} \varepsilon (a_{i,k} a_{i,k}^\dagger - b_{i,k} b_{i,k}^\dagger) + \sum_{(a_i,k,b_j,k)} (t_n a_{i,k} b_{j,k}^\dagger + \text{H.c.}) \quad (1)$$

where  $a$  ( $b$ ) and  $a^\dagger$  ( $b^\dagger$ ) are the annihilation and creation operators on the sublattice sites,  $\varepsilon$  represents the on-site energy difference. Each lattice is specified by subscripts  $(i, k)$ , where the first labels the position in each layer and the second labels the number of layers. The first term in equation (1) represents the sublattice on-site energy difference. The second term represents the intralayer hopping between nearest sublattices. The intralayer hopping  $t_n$  is real and constant. The first Brillouin zone (BZ) of this lattice is shown in Fig. 1c. As this system is periodic along the  $z$  direction,

$k_z$  is a good quantum number. For each fixed  $k_z$ , and if we consider the dispersion and transport in the  $x$ - $y$  plane, the 3D system can be reduced to an effective two-dimensional (2D) system with a unit cell, as shown in Fig. 1b. The corresponding first BZ is illustrated in Fig. 1d, which represents a plane cut with the specified  $k_z$  in the original first BZ in Fig. 1c.

We can now introduce different kinds of interlayer coupling, from which we choose two special examples (Fig. 1e,g, where hopping is non-zero only between connected sites). In Fig. 1e, the hopping amplitudes are different for the two different sublattices. In this case, the interlayer hopping part  $H_1$  is given by

$$H_1 = \sum_{(i,k)} (t_a a_{i,k} a_{i,k+1}^\dagger + t_b b_{i,k} b_{i,k+1}^\dagger + \text{H.c.})$$

where  $t_a$  and  $t_b$  ( $t_a \neq t_b$  and both are real) represent the interlayer hopping terms for sublattices  $a$  and  $b$ . The corresponding Bloch Hamiltonian  $H(\mathbf{k})$  is given by

$$H(\mathbf{k}) = \begin{pmatrix} \varepsilon + 2t_a \cos(k_z d_h) & t_n \beta \\ (t_n \beta)^* & -\varepsilon + 2t_b \cos(k_z d_h) \end{pmatrix} \quad (2)$$

where  $\beta = \exp(-ik_x a) + 2 \cos(\sqrt{3}k_y a/2) \exp(ik_x a/2)$ ,  $a$  is the distance between the two sublattices,  $d_h$  is the interlayer distance and  $\mathbf{k} = (k_x, k_y, k_z)$  is the Bloch wavevector. The eigenvalue of  $H(\mathbf{k})$  is given by  $E = (t_a + t_b) \cos(k_z d_h) \pm \sqrt{[t_n \beta]^2 + [\varepsilon + (t_a - t_b) \cos(k_z d_h)]^2}$ . The first term under the square vanishes along the KH line. If  $[\varepsilon + (t_a - t_b) \cos(k_z d_h)]$  is non-zero, the inversion symmetry of the reduced 2D hexagonal lattice is broken, as illustrated in Fig. 1f. When  $|t_a - t_b| > \varepsilon$ , there exist special values  $k_z = \pm \arccos[\varepsilon / (t_b - t_a)] / d_h$ , where  $H(x, y, k_z) = H(-x, -y, k_z)$ . This implies that Dirac cones can form in the  $k_x$ - $k_y$  plane for these values of  $k_z$ . These special points can give rise to Weyl points in the 3D band structure, as we will discuss later.

Another interesting example is shown in Fig. 1g, in which we consider a chiral kind of interlayer coupling. We will see that if we consider the propagation in the  $x$ - $y$  plane for a fixed  $k_z$ , this is effectively a realization of the topological Haldane model<sup>2</sup>. The interlayer coupling coefficients as indicated by the cyan bonds in Fig. 1g are denoted by  $t_c$ , which are taken to be identical and real. For a fixed  $k_z$ , the interlayer hopping becomes next-nearest-neighbour hopping in the reduced 2D system, with a complex hopping coefficient  $t_c e^{i\phi}$ , where  $\phi = \pm k_z d_h$  depends on whether the hopping proceeds in the clockwise or anticlockwise direction. In Fig. 1h, we use red arrows to indicate the direction along which  $\phi = -k_z d_h$ . After a complete loop of hopping in the direction indicated, the total phase accumulated is  $-3k_z d_h$ . This means the gauge flux enclosed by this loop is  $-3k_z d_h$ . In Fig. 1h, we use

Department of Physics and Institute for Advanced Study, Hong Kong University of Science and Technology, Clear Water Bay, Hong Kong, China. <sup>†</sup>These authors contributed equally to this work. \*e-mail: phchan@ust.hk

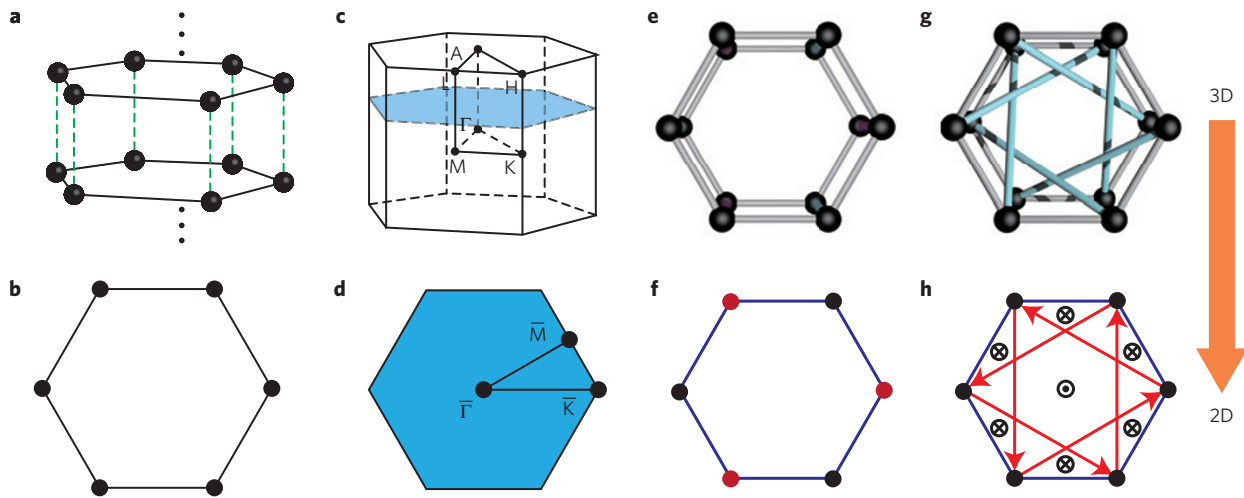


**Figure 1 | Interlayer coupling induces different symmetry breakings in two-dimensional systems.** **a, b**, AA stacking of a hexagonal lattice (**a**) and its unit cell (**b**). **c**, Reciprocal space of the system shown in **a**. **d**, Reduced first Brillouin zone for each fixed  $k_z$ . Different interlayer couplings introduce different effects in the reduced two-dimensional lattice. **e, f**, Unequal interlayer coupling at different sublattice sites corresponds to broken inversion symmetry in 2D. **g, h**, Chiral interlayer coupling generates an effective gauge flux at each fixed  $k_z$ . The red arrows in **h** represent the direction of positive phase hopping, and dotted and crossed black circles represent the direction of local flux. This is an analogue of the Haldane model.

dotted and crossed black circles to represent the sign of local flux. Although the total flux inside each unit cell is zero, we have non-zero local flux. The chiral interlayer coupling introduces Peierls phase<sup>27</sup> (Supplementary Information II) for the hopping parameters in 2D for any non-zero  $k_z$ , thereby achieving a staggered synthetic gauge flux in a 'static' system. This is different from the standard paradigm of using dynamical perturbation to induce synthetic gauge flux<sup>17</sup>. For a system with both the coupling shown in Fig. 1e and that in Fig. 1g, one can then tune the system across a topological transition point by changing the value of  $(t_a - t_b)/t_c$  or  $k_z$ . The phase diagram is shown in Supplementary Information I.

### Breaking of inversion symmetry

Let us now consider real acoustic systems. We start with a periodic array of acoustic cavities linked together by tubes, as shown in Fig. 2a (top view) and b (side view). The resonance cavities can be viewed as 'meta-atoms' and the hopping strength between the meta-atoms can be tuned by changing the radius of the connecting tubes. The light blue colour in Fig. 2b denotes the area where the hard boundary condition is applied and the system is filled with air. The intralayer couplings are set to be equal by giving all horizontal connecting tubes the same radius ( $w_0$ ). The interlayer couplings (along the  $z$  direction) are set to different values by choosing different radii ( $w_1 \neq w_2$ ) for different sublattice sites. Here we consider the mode (Fig. 2c) whose pressure is described by a sinusoidal function along the  $z$  direction and does not vary in the horizontal plane. We note here that different mode profiles give basically the same results, except that the working frequency will be different. In Fig. 2d, we show the band dispersions of this mode in the  $k_x$ - $k_y$  plane with different values of  $k_z$ . At  $k_z = 0$  (red lines in Fig. 2d), the dispersion in the  $k_x$ - $k_y$  plane has a gap at the  $\bar{K}$  point owing to inversion symmetry breaking. As this reduced 2D system still has mirror symmetry with respect to the  $x$ - $z$  plane, the Berry curvature is an odd function in the reciprocal space and the two red bands are topologically trivial, with zero Chern numbers. At  $k_z = 0.623$ , there is a Dirac point at  $\bar{K}$ , as shown by the black lines in Fig. 2d, consistent with the tight-binding model's prediction that degeneracy for the reduced 2D system can be recovered at some finite  $k_z$  value. The value of  $k_z$ , where the system has a Dirac cone in the  $k_x$ - $k_y$  plane, is slightly different from the tight-binding prediction. This is because the introduction of the connecting tubes changes the resonance

frequency of the cavities, which is equivalent to  $\varepsilon \neq 0$  in equation (2). In Fig. 2e, we show the band dispersion (black curves) along the KH direction ( $z$  direction). The difference in frequency between the two bands along  $k_z$  reflects the strength of inversion symmetry breaking as a function of  $k_z$ . As shown in Fig. 2e, the band dispersion near the Dirac point in Fig. 2d is also linear along the  $z$  direction, indicating that the degeneracy point is a Weyl point<sup>24–26,28</sup> in the 3D band structure.

### Synthetic gauge flux

We now consider the realization of effective acoustic gauge flux. In fact, creating effective acoustic gauge flux for a fixed  $k_z$  with chiral interlayer coupling can go beyond the tight-binding description. Figure 3a,b shows the top and side views of a unit cell of an acoustic system that exhibits synthetic gauge flux. The chiral coupling is characterized by the relative rotation angle  $\theta$  between the holes on the upper and lower boundaries of the planar ( $x$ - $y$  plane) waveguides. When  $\theta = 0$ , the coupling is non-chiral and the synthetic gauge flux vanishes. The strength of the gauge flux depends on the rotational angle as well as the radius of the connecting tube  $r_1$  (Supplementary Information IV).

We consider the lowest-order acoustic mode and, as before, the waveguide is filled with air. In Fig. 3c, red/black curves indicate the band dispersion in the reduced 2D BZ at  $k_z \neq 0/k_z = 0$ , representing the system with/without the effective gauge flux. The degeneracy at  $\bar{K}$  is lifted by the gauge flux. The effect of this synthetic gauge flux can also be seen from the Chern number of each isolated band, which is found to be  $+1/-1$  for the lower/upper band when  $k_z$  is positive. The strength of the gauge flux can be seen from the width of the gap at the  $\bar{K}$  point. In Fig. 3d, we show the band dispersion along the KH direction. The two bands are required to be degenerate at the K and H points by a combination of time-reversal and  $C_6$  rotational symmetry. Along the KH line, the two states repel and the width of the gap reaches its maximum near the middle of the KH line.

A non-zero Chern number for a non-zero  $k_z$  implies the existence of a topologically protected chiral edge mode in the boundary between this system and a topologically trivial system inside the common gap region. We construct a hexagonal ribbon with finite width along the  $y$  direction and periodic along the  $x$  direction (see Supplementary Information V). We use hard boundaries to confine

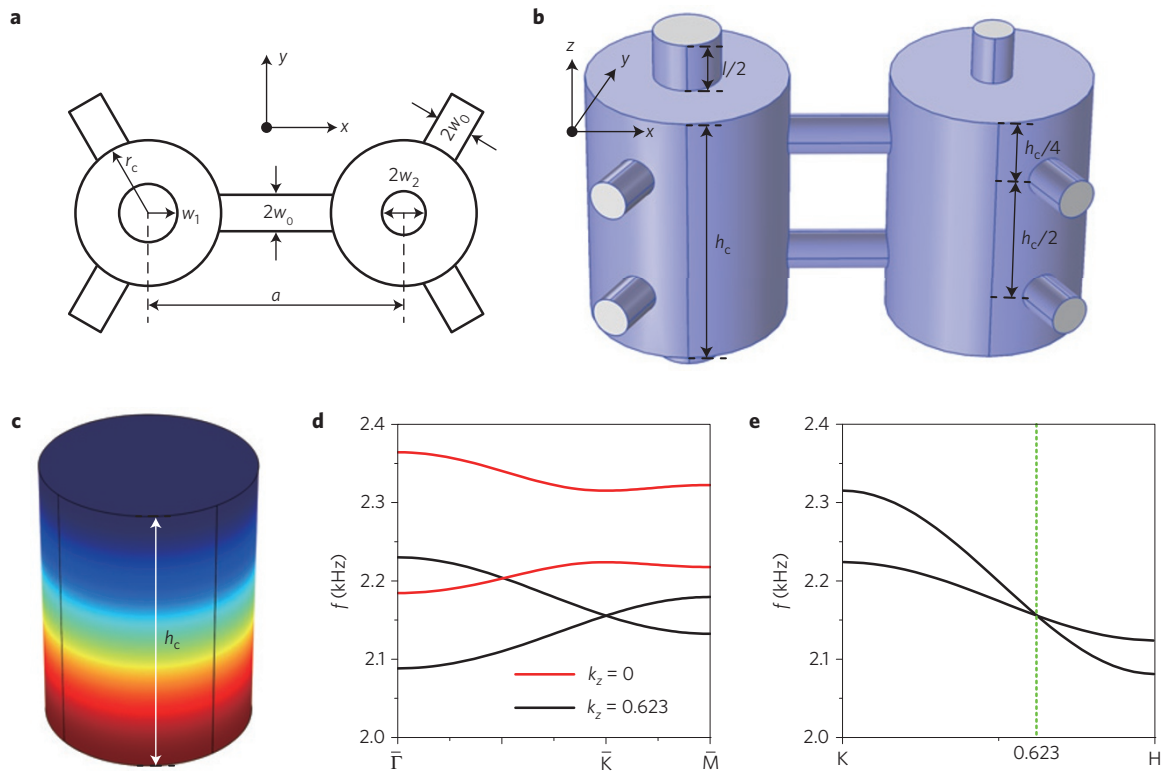


**Figure 2 | Different interlayer coupling coefficients induce effective breaking of in-plane inversion symmetry. a, b**, Top and side views, respectively, of a unit cell of the acoustic system. **c**, Real part of the eigenpressure field of a cavity mode for a single resonator at 2,144 Hz, where red and blue represent positive and negative pressure, respectively. **d**, Band dispersion of the cavity mode in **c** for different values of  $k_z$ , where the black curves have a Dirac point at  $\bar{K}$  for a special value of  $k_z$  and the degeneracy is lifted (red curves) otherwise. The Chern number of the two red bands are both  $C=0$ . **e**, Band dispersion along the KH direction. The two bands cross at a special point ( $k_z = 0.623$  with normalized unit  $\pi/(h_c + l)$ ). This special point corresponds to a Weyl point of this acoustic system.

the sound wave in the  $y$  direction to within the acoustic system. The hard boundary condition can be regarded as a trivial band gap with zero decay length. Figure 3e shows the projection band (grey) along the  $x$  direction and the dispersions of two surface states with  $k_z = 0.5\pi/(h_c + l)$ . The red and blue colours denote surface states localized at the lower and upper boundaries in the  $y$  direction, respectively (see Supplementary Information V). The two degeneracy points in Fig. 3d correspond to Weyl points<sup>24–26,28</sup> in the 3D band structure. If we consider a surface BZ spanned by  $k_x$  and  $k_z$ , the allowed boundary modes for a given excitation frequency will trace out trajectories connecting two Weyl points that are analogous to ‘Fermi arcs’ in electronic Weyl semi-metals<sup>25,28,29</sup> (see Supplementary Information VI). If the width of the ribbon is large enough (larger than the decay length of the edge state), the edge state localized at one boundary cannot be scattered backwards as long as  $k_z$  is still preserved. In Fig. 3f, we show the property of the edge state. The edge state is excited on the left boundary (marked by the purple star) inside the gap region, and propagates clockwise around the corners and the defect without being backscattered. Black and purple arrows are drawn to show the direction of propagation of the sound wave. The direction, either clockwise or anticlockwise, depends on the sign of  $k_z$ . We supplemented our full wave simulation for an infinite system (with periodic boundary conditions) with simulations using a 3D finite-sized tight-binding model (Supplementary Information III). Different from the one-way edge states of 2D acoustic systems published recently<sup>20</sup>, the time-reversal symmetry in our 3D system is preserved. We note that the time-reversal partner of a clockwise state for a particular  $k_z$  is an anticlockwise state at  $-k_z$ .

### Weyl points

This synthetic gauge flux is related to the Weyl points. In 3D, Weyl point dispersion is governed by the Weyl Hamiltonian  $H(\mathbf{k}) = \sum k_i v_{ij} \sigma_j$ ,  $i, j \in \{x, y, z\}$  (refs 24–26,28,30–32), where  $v_{ij}$  are the group velocities and  $\sigma_j$  are the Pauli matrices. Weyl points have associated topological charges (or chirality,  $c = \text{sgn}[\det(v_{ij})] = \pm 1$ ), which can be regarded as monopoles of Berry flux<sup>26</sup>. In Fig. 4a,b, we show the Weyl points of the two acoustic systems considered in Figs 2 and 3, respectively. The systems considered in Fig. 2 have mirror symmetry with respect to the  $x$ - $z$  plane, which ensures that the two mirror-symmetric Weyl points in the reciprocal space have charges with opposite signs, and hence the net charge in the horizontal light blue plane in Fig. 4a is zero. For any 2D band with an arbitrary (but fixed) value of  $k_z$ , the net Berry flux vanishes and its Chern number is zero. In contrast, the system with chiral coupling (for example, Fig. 3) does not possess mirror symmetry and the remaining  $C_6$  symmetry ensures all the Weyl points on the same  $k_z$  plane have charges with the same sign. Meanwhile, the net charge of Weyl points inside the first BZ must vanish<sup>29</sup>, which means there must be at least two planes with different  $k_z$  possessing Weyl points of different charges. For example, the  $k_z d_h/\pi = 0$  and  $k_z d_h/\pi = \pm 1$  planes in Fig. 4b carry net topological charges of  $+2$  and  $-2$  respectively. Thus, for an arbitrary fixed  $k_z$  lying between these two planes, the net Berry flux through the reduced 2D BZ is  $2\pi$  and the Chern number is  $\pm 1$ , with the sign determined by the sign of  $k_z$  (refs 24,25,29). The chiral coupling guarantees the non-zero Chern number, which corroborates the existence of a synthetic gauge flux.

Our idea of manipulating acoustic waves can also be extended to electromagnetic wave systems. The vector property of electromagnetic waves as well as the possibility of breaking

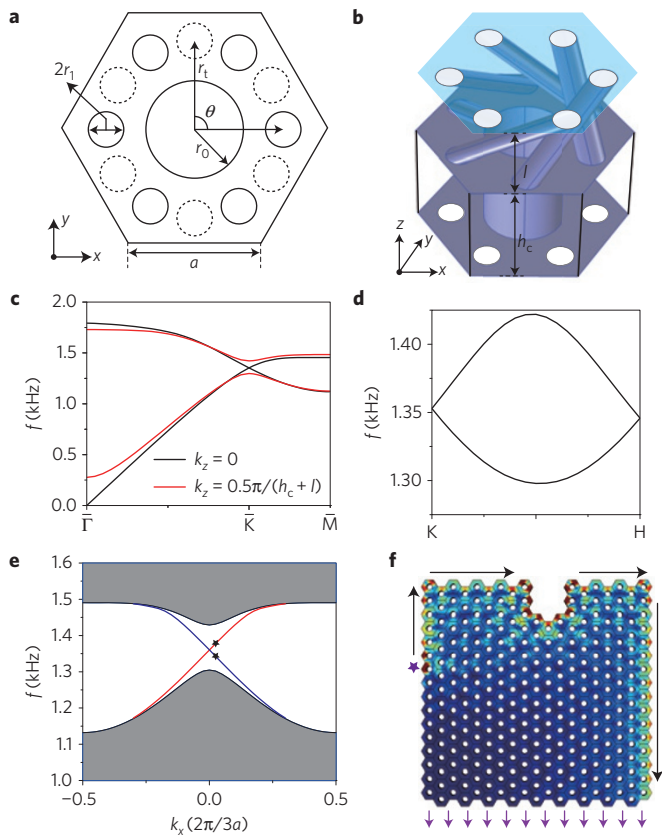


**Figure 3 | Chiral interlayer coupling induces a synthetic gauge flux.** **a, b**, Top view and side views, respectively, of a unit cell of the acoustic system. The dashed circles and solid circles in **a** represent the holes opened at the upper and lower sides of the in-plane ( $x$ - $y$ ) sound waveguide, respectively.  $\theta$  represents the rotation angle of the connecting tubes. **c**, Band dispersion of the lowest mode for two values of  $k_z$ , where the black/red curves represent bands without/with the effective gauge flux. The Chern numbers of the two red bands are  $C = +1$  (lower band) and  $C = -1$  (upper band). The sign of Chern numbers can be changed by reversing the sign of  $k_z$ . **d**, Band dispersion along the KH direction in the reciprocal space. K and H points are Weyl points of the 3D band structure. The strength of the synthetic gauge flux reaches its maximum near  $k_z = 0.5\pi/(h_c + l)$ . **e**, Projection band (grey) along the  $x$  direction with  $k_z = 0.5\pi/(h_c + l)$ . Red and blue curves represent the surface states localized at the lower and upper boundaries of a ribbon, respectively (see Supplementary Fig. 5, in which the eigenpressure fields of the states marked by the black stars are shown). **f**, The surface wave for  $k_z = -0.5\pi/(h_c + l)$  propagates in the clockwise direction around the corners and the defect of a finite system without being backscattered. The purple star marks the position of our sound source, the black arrows illustrate the direction of propagation of the sound wave inside the system and the purple arrows at the bottom show the coupling of the sound wave from the boundary of the system to the outside.

time-reversal symmetry using magnetic fields in electromagnetic systems can offer more flexibility in introducing interesting phenomena such as analogues of chiral anomaly<sup>33</sup>. The results shown in Figs 2 and 3 demonstrate separately and respectively the consequences of on-site coupling difference and chiral coupling. If both symmetry-breaking mechanisms are simultaneously incorporated in the design of the acoustic meta-crystal, we can in principle enter all the regimes in the phase diagram of the Haldane model as we vary  $k_z$ . The effective gauge flux induced by chiral coupling may stimulate new ideas for manipulating sound wave propagation, and may have implications in fields such as sound signal processing, sound energy harvesting, and noise protection.

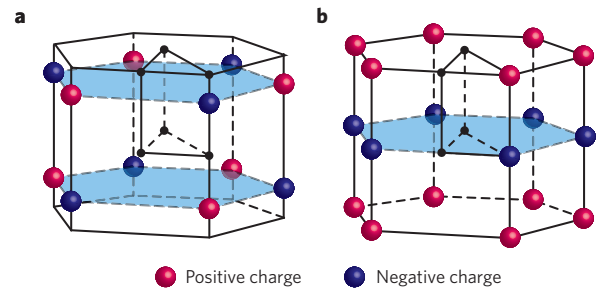


**Figure 4 | Weyl points in the reciprocal space.** **a, b** Weyl points for the acoustic systems studied in Figs 2 and 3, respectively. The red and blue spheres represent Weyl points with positive and negative topological charges, respectively.

**Methods**

Methods and any associated references are available in the [online version of the paper](#).

Received 28 April 2015; accepted 3 August 2015; published online 7 September 2015

**References**

1. Klitzing, K. v., Dorda, G. & Pepper, M. New method for high-accuracy determination of the fine-structure constant based on quantized Hall resistance. *Phys. Rev. Lett.* **45**, 494–497 (1980).
2. Haldane, F. D. M. Model for a quantum Hall effect without Landau levels: Condensed-matter realization of the “Parity Anomaly”. *Phys. Rev. Lett.* **61**, 2015–2018 (1988).
3. Hasan, M. Z. & Kane, C. L. Colloquium: Topological insulators. *Rev. Mod. Phys.* **82**, 3045–3067 (2010).
4. Qi, X.-L. & Zhang, S.-C. Topological insulators and superconductors. *Rev. Mod. Phys.* **83**, 1057–1110 (2011).
5. Haldane, F. D. M. & Raghu, S. Possible realization of directional optical waveguides in photonic crystals with broken time-reversal symmetry. *Phys. Rev. Lett.* **100**, 013904 (2008).
6. Wang, Z., Chong, Y., Joannopoulos, J. D. & Soljačić, M. Observation of unidirectional backscattering-immune topological electromagnetic states. *Nature* **461**, 772–775 (2009).
7. Wang, Z., Chong, Y. D., Joannopoulos, J. D. & Soljačić, M. Reflection-free one-way edge modes in a gyromagnetic photonic crystal. *Phys. Rev. Lett.* **100**, 013905 (2008).
8. Rechtsman, M. C. *et al.* Photonic Floquet topological insulators. *Nature* **496**, 196–200 (2013).
9. Hafezi, M., Demler, E. A., Lukin, M. D. & Taylor, J. M. Robust optical delay lines with topological protection. *Nature Phys.* **7**, 907–912 (2011).
10. Hafezi, M., Mittal, S., Fan, J., Migdall, A. & Taylor, J. M. Imaging topological edge states in silicon photonics. *Nature Photon.* **7**, 1001–1005 (2013).
11. Khanikaev, A. B. *et al.* Photonic topological insulators. *Nature Mater.* **12**, 233–239 (2013).
12. Chen, W.-J. *et al.* Experimental realization of photonic topological insulator in a uniaxial metacrystal waveguide. *Nature Commun.* **5**, 6782 (2014).
13. Liang, G. Q. & Chong, Y. D. Optical resonator analog of a two-dimensional topological insulator. *Phys. Rev. Lett.* **110**, 203904 (2013).
14. Lu, L., Joannopoulos, J. D. & Soljačić, M. Topological photonics. *Nature Photon.* **8**, 821–829 (2014).
15. Skirlo, S. A., Lu, L. & Soljačić, M. Multimode one-way waveguides of large Chern numbers. *Phys. Rev. Lett.* **113**, 113904 (2014).
16. He, W.-Y. & Chan, C. T. The emergence of Dirac points in photonic crystals with mirror symmetry. *Sci. Rep.* **5**, 8186 (2015).
17. Fang, K., Yu, Z. & Fan, S. Realizing effective magnetic field for photons by controlling the phase of dynamic modulation. *Nature Photon.* **6**, 782–787 (2012).
18. Prodan, E. & Prodan, C. Topological phonon modes and their role in dynamic instability of microtubules. *Phys. Rev. Lett.* **103**, 248101 (2009).
19. Xiao, M. *et al.* Geometric phase and band inversion in periodic acoustic systems. *Nature Phys.* **11**, 240–244 (2015).
20. Yang, Z. *et al.* Topological acoustics. *Phys. Rev. Lett.* **114**, 114301 (2015).
21. Kane, C. L. & Lubensky, T. C. Topological boundary modes in isostatic lattices. *Nature Phys.* **10**, 39–45 (2014).

22. Fleury, R., Sounas, D. L., Sieck, C. F., Haberman, M. R. & Alù, A. Sound isolation and giant linear nonreciprocity in a compact acoustic circulator. *Science* **343**, 516–519 (2014).
23. Jotzu, G. *et al.* Experimental realization of the topological Haldane model with ultracold fermions. *Nature* **515**, 237–240 (2014).
24. Lu, L., Fu, L., Joannopoulos, J. D. & Soljačić, M. Weyl points and line nodes in gyroid photonic crystals. *Nature Photon.* **7**, 294–299 (2013).
25. Wan, X., Turner, A. M., Vishwanath, A. & Savrasov, S. Y. Topological semimetal and Fermi-arc surface states in the electronic structure of pyrochlore iridates. *Phys. Rev. B* **83**, 205101 (2011).
26. Fang, Z. *et al.* The anomalous Hall effect and magnetic monopoles in momentum space. *Science* **302**, 92–95 (2003).
27. Hofstadter, D. R. Energy levels and wave functions of Bloch electrons in rational and irrational magnetic fields. *Phys. Rev. B* **14**, 2239–2249 (1976).
28. Burkov, A. A. & Balents, L. Weyl semimetal in a topological insulator multilayer. *Phys. Rev. Lett.* **107**, 127205 (2011).
29. Yang, K.-Y., Lu, Y.-M. & Ran, Y. Quantum Hall effects in a Weyl semimetal: Possible application in pyrochlore iridates. *Phys. Rev. B* **84**, 075129 (2011).
30. Lu, L. *et al.* Experimental observation of Weyl points. *Science* **349**, 622–624 (2015).
31. Xu, S.-Y. *et al.* Discovery of a Weyl fermion semimetal and topological Fermi arcs. *Science* **349**, 613–617 (2015).
32. Lv, B. Q. *et al.* Experimental discovery of Weyl semimetal TaAs. *Phys. Rev. X* **5**, 031013 (2015).
33. Nielsen, H. B. & Ninomiya, M. The Adler–Bell–Jackiw anomaly and Weyl fermions in a crystal. *Phys. Lett. B* **130**, 389–396 (1983).

### Acknowledgements

The authors would like to thank Z. Q. Zhang and K. T. Law for discussions. This work was supported by the Hong Kong Research Grants Council (grant no. AoE/P-02/12).

### Author contributions

C.T.C. initiated the programme. M.X. and W.-J.C. contributed equally to this work. All authors contributed to the analysis and discussion of the results.

### Additional information

Supplementary information is available in the online version of the paper. Reprints and permissions information is available online at [www.nature.com/reprints](http://www.nature.com/reprints). Correspondence and requests for materials should be addressed to C.T.C.

### Competing financial interests

The authors declare no competing financial interests.

## Methods

All simulations were performed using the commercial solver package COMSOL Multiphysics. The 3D geometry was implemented by imposing periodic boundary conditions on some specified boundaries. The systems were filled with air (density  $\rho = 1.3 \text{ kg m}^{-3}$  and speed of sound  $v = 343 \text{ m s}^{-1}$ ). Eigenmode calculations were carried out to find the band structures as well as eigenmodes in Figs 2c–e and 3c–e. Frequency domain calculations were carried out to find the  $k_z$  conserved backscattering immune transport behaviour of the edge mode shown in Fig. 3f.

Figure 2a and b, respectively, show the top view and side view of the unit cell studied in Fig. 2. The parameters used were  $r_c = 3 \text{ cm}$ ,  $a = 9 \text{ cm}$ ,  $w_0 = w_2 = 0.6 \text{ cm}$ ,  $w_1 = 1 \text{ cm}$ ,  $h_c = 8 \text{ cm}$  and  $l = 3 \text{ cm}$ . The light blue colour in Fig. 2b denotes the area where the hard boundary condition was applied, and the white colour indicates the area where the periodic boundary condition was applied with a given Bloch wavevector. Figure 2c shows the real part of the pressure field of a cavity mode found at 2,144 Hz, where the parameters of the cavity were the same as before—that is,  $r_c = 3 \text{ cm}$  and  $h_c = 8 \text{ cm}$ . The hard boundary condition was applied over all the cavity boundaries and the eigenmode calculation was then performed to find the eigenpressure distribution, where the red/blue colour indicates positive/negative local pressure.

Figure 3a and b, respectively, show the top and side views of the unit cell studied in Fig. 3. The parameters of the unit cell were  $r_0 = 3 \text{ cm}$ ,  $r_1 = 5.5 \text{ cm}$ ,  $a = 8 \text{ cm}$ ,  $r_2 = 1.2 \text{ cm}$ ,  $\theta = 90^\circ$ ,  $l = 5 \text{ cm}$ ,  $h_c = 8 \text{ cm}$ . The dashed circles and solid circles in Fig. 3a represent the holes opened at the upper and lower sides of the sound waveguide in the  $x$ – $y$  plane, respectively.  $\theta$  represents the rotation angle of the connecting tubes. In Fig. 3b, the light blue colour marks the area where the hard

boundary condition was applied, and solid white circles represent areas where Floquet periodic boundary conditions were applied with a given Bloch wavevector. Floquet periodic boundary conditions were also applied to the side walls (they are transparent to expose the interior structure of the unit cell). To calculate the projection band shown in Fig. 3e, we constructed a ribbon with finite length (16 unit cells) along the  $y$  direction. Floquet periodic boundary conditions were then applied to the side walls in the  $x$  and  $z$  directions. The remaining boundaries were all set as hard boundaries. The Bloch wavevector along the  $z$  direction was fixed at  $k_z = 0.5\pi/(l + h_c)$  in this calculation. In Fig. 3f, the purple star marks the position of our source. To couple waves inside our system, we adopted the plane wave radiation boundary condition for one of the side boundaries of a unit cell with a plane wave excited at this port and a working frequency of 1,360 Hz. All the side boundaries in the negative  $y$  direction were also set as plane wave radiation boundaries to couple waves outside of our system, and we used purple arrows to indicate the direction of wave propagation through these ports. Here the ‘plane wave radiation boundary’ plays two roles in our simulation. The one at the side boundary serves as the source and those in the negative  $y$  direction at the bottom are used to couple the wave from our system to the outside so that the surface wave will not go around all the side boundaries and back to the source port boundary. The plane wave radiation boundary, which serves as source, can also be replaced by other kinds of source, such as a line source. All the boundaries on the upper and lower sides in the  $z$  direction are set as Floquet periodic boundary conditions with a Bloch wavevector along the  $z$  direction given by  $k_z = -0.5\pi/(l + h_c)$ , where the ‘+’ or ‘−’ sign of  $k_z$  determines the direction (clockwise or anticlockwise) of surface wave propagation. All the remaining boundaries are set as hard boundaries.